Asian Journal of Chemistry; Vol. 37, No. 1 (2025), 53-60

ASIAN JOURNAL OF CHEMISTRY

https://doi.org/10.14233/ajchem.2025.32789

Novel $MgFe_2O_4/TiO_2/ZnO$ Nanocomposites Synthesized by Sol-Gel Method for Visible Light Photocatalytic Degradation of Eosin Y Dye

Ch. Ramya Kumari*, K. Jyothi Priya, M. Suneetha, N. Sridevi Chandrakala, T. Bulli Babu, M. Padma and S. Paul Douglas*

Department of Engineering Chemistry, AU College of Engineering, Andhra University, Visakhapatnam-530003, India

*Corresponding authors: E-mail: ramyametta99@gmail.com; spdfchem@andhrauniversity.edu.in

Received: 27 September 2024; *Accepted*: 22 November 2024; *Published online*: 31 December 2024; AJC-21851

The synthesized magnesium ferrite-titania-zinc oxide nanocomposites are extremely successful in the photocatalytic degradation of eosin Y dye because of their size, stability, structure, eco-friendliness and high efficiency. The UV-visible, XRD, SEM, TEM, FTIR and VSM techniques were used to analyze the structure of the nanocomposites. The value of band gap energy for nanocomposite is 2.3 eV. The synthesized nanocomposites were investigated for their efficiency in degrading eosin Y dye under visible light, with studies conducted at different time intervals and evaluation of catalyst reusability. The obtained nanocomposites exhibit an extensive surface area, which facilitates numerous active sites for interactions between the dye molecules and the metal oxide nanoparticles when exposed to visible light. The antibacterial activity of the prepared nanocomposites were also conducted against Gram-negative *Aeromonas* and Gram-positive *Firmicutes* and the results have shown very efficient antibacterial activity.

Keywords: $MgFe_2O_4/ZnO/TiO_2$ nanomagnetic composites, Visible-light photodegradation, Eosin Y dye.

INTRODUCTION

Reliable access to clean water and energy is essential for human beings and sustainable economic development. With water scarcity emerging as a global challenge, treating wastewater for reuse in industries, agriculture and animal feed has become vital for conserving potable water supplies [1]. Organic compounds are widely employed in industrial operations including fabric, leather, textiles, medicines, food processing and paper manufacture. However, they are toxic, non-biodegradable, carcinogenic and harmful to the environment, posing risks to human health [2]. Eosin Y, commonly referred to as eosin, is a water-soluble crystalline pigment, characterized by a yellowish red colour with greenish fluorescence and a member of the xanthine group [3]. Eosin Y was one of the most significant dyes due to its relatively short duration of original state. Moreover, it demonstrated significant consistency and provided a valuable analysis for the elimination of both photoreactions and oxidation [4].

Many of the chemicals and dyes used in textile processes are not biodegradable, creating significant aesthetic issues for the public and limiting the reuse of wastewater. Biological treatment alone is not an ideal solution, as it has several drawbacks, including sludge generation, high energy costs and frequent maintenance requirements [5]. Currently, wastewater treatment involves various methods to remove these chemicals, including chemical, biological and physical processes. Chemical processes, such as advanced oxidation, ozonation and electrocoagulation, are commonly used but often considered unfavourable due to their high cost [6]. A significant hurdle in separation processes is the necessity to eliminate pollutants thoroughly once extracted from the wastewater. In contrast, well-designed oxidation based methods frequently provide a more comprehensive approach to address the issue of pollutant elimination [7].

Photocatalysis is one of the most effective methods for decolourizing and detoxifying the industrial effluents [8,9]. This process degrades the organic dyes and contaminants rather than altering them, making it most suitable. Thus, the organic dyes, coloured chemicals, insecticides and herbicides can be converted into environmentally benign products using this method. A key advantage of photocatalysis is that it harnesses

solar energy as a natural component [10]. The effectiveness of photocatalytic processes is largely determined by key features of the photocatalysts including (i) surface area, which influences the adsorption and (ii) shape, which affects the electron-hole recombination rate. However, despite its environmental benefits, the practical application of this promising technology is significantly hindered by the low separation efficiency of photogenerated charge carriers during the photocatalytic process [11].

Researchers worldwide are actively working to develop more advanced semiconducting nanostructures to effectively remove contaminants from the polluted water. Titanium dioxide (TiO_2) is a highly regarded material in nanoscience and nanotechnology due to its exceptional properties, including low cost, high stability, biocompatibility, non-toxicity, chemical inertness, high refractive index and wide band gap [12,13]. Titanium dioxide has been shown to exhibit enhanced photoelectrochemical performance and highly efficient photocatalytic properties [14]. Similarly, zinc oxide (ZnO) has also attracted significant attention among semiconductor photocatalysts due to its wide band gap (3.2 eV), low cost, non-toxicity and high chemical stability. However, it faces several major challenges like photo-corrosion and rapid electron-hole recombination, which greatly reduce its photoactivity and photostability. Due to its large band gap, ZnO can only utilize a small fraction of UV light–less than 5% of solar radiation in photocatalytic reactions [15]. Since the photodegradation mechanism of ZnO resembles that of TiO_2, it serves as a suitable substitute for TiO_2. In fact, studies have shown that ZnO demonstrates greater photocatalytic efficacy than TiO_2 [16]. With a threshold of 425 nm, ZnO can absorb a larger proportion of UV light compared to TiO_2. Consequently, researchers can use ZnO/TiO_2 nanocomposites as photocatalysts in aqueous systems to effectively degrade or decolourize organic dyes when exposed to sunlight [17]. Both substances tend to aggregate significantly, especially at high concentrations. To address the aggregation problem and enhance photocatalytic activity, various materials such as metal ferrites, biopolymers and carbon materials, can be incorporated into semiconductors as solid supports. However, significant challenges in the separation and recycling of exhausted photocatalysts persist. Immobilizing catalysts on solid supports is crucial for overcoming these challenges.

Nanostructures of magnetic materials have recently received a lot of interest because of their distinct characteristics, which differ significantly from their bulk counterparts [18]. Furthermore, studies have shown that support materials can increase the surface area of catalysts, thereby enhancing their hydrophobicity, thermal stability, hydrolytic stability and chemical stability [19]. The magnetic properties of the tiny metal ferrites facilitate their removal from aqueous solutions. For instance, manganese and nickel ferrites remain relatively stable and exhibit low band gaps. However, pure metal ferrites encounter challenges due to rapid electron-hole pair recombination, which limits their effectiveness. One effective solution to this problem involves using composites that incorporate carbonaceous materials as support [20]. Magnesium ferrite ($MgFe_2O_4$), a significant ferrite with a cubic normal spinel structure, is a soft magnetic n-type semiconductor.

The sol-gel template approach remains one of the most advanced ways for producing mesoporous oxides [21]. When paired with the widely used solvo(hydro)thermal processing of an intermediate amorphous organo-inorganic product, this approach enables researchers to regulate the formation of various forms and textures at the nanoscale [22]. This work shows that magnetic ferrite-based titanium oxide and zinc oxide nanocomposites may degrade organic dyes in wastewater and water. Although numerous studies have examined the potential of ferrite-based photocatalysts for wastewater treatment, there are currently no comprehensive evaluations of their application in integrated photocatalytic methods. Thus, herein, the sol-gel technique was used to synthesize nanocomposite consisting of trimetallic materials ($MgFe_2O_4$-ZnO-TiO_2) from their components. The prepared nanocomposite was characterized through different spectroscopic and microscopic techniques. Finally, the prepared nanocomposite was then utilized as photocatalyst for the degradation of eosin Y dye.

EXPERIMENTAL

The chemicals used in this work were zinc nitrate, ethylene glycol, magnesium nitrate, ferric citrate, citric acid, titanium tetrachloride, hydrochloric acid and procured from different commerical sources with highest purity.

Synthesis of magnesium ferrite: The solutions of magnesium nitrate (4.23 g in 10 mL distilled water) and ferric citrate (71.64 g in 10 mL distilled water) were prepared separately. Added 12.6 g of citric acid to both solutions followed by the gradual addition of ammonia to each beaker to maintain a neutral pH. Mixed the two solutions slowly, added 20 mL of ethylene glycol while stirring and then heated the mixture on a hot plate until it forms a dry powder. The obtained powder was calcined at 800 ºC for 2 h to obtain finely powdered nano magnesium ferrite.

Synthesis of titania nanocomposites: A white and curdy precipitate was formed by gradual addition of 6.9 mL of $TiCl_4$ to a beaker containing 350 mL of distilled water and 0.5 mL of HCl. The beaker was then covered with aluminum foil. After the formation of precipitate, stirred it for 1 h and then subsequently heated on a hot plate at 80-100 ºC range, which resulted in the formation of fine powder.

Synthesis of zinc oxide nanocomposites: Mixed 20 mL of ethylene glycol with 5 g of zinc nitrate and stirred for 1 h to achieve a homogeneous solution. The mixture was allowed to stand at room temperature for 1 day until it forms a gel. Then, the gel was heated on a hot plate, calcined at 500 ºC for 2 h and then, grinded the material to obtain a fine powder.

Synthesis of $MgFe_2O_4$/TiO_2/ZnO ternary nanocomposite: The ternary nanocomposite was prepared by mixing the components *viz.* 0.8 g of $MgFe_2O_4$, 0.1 g of TiO_2 and 0.1 g of ZnO thoroughly and grinded them into a fine powder using a mortar and pestle.

Characterization: The ternary nanocomposite ($MgFe_2O_4$/TiO_2/ZnO) was analyzed using infrared spectroscopy (IR Prestige 21) in the 4000-500 cm^{-1} range using KBr pellets. The X-ray diffraction (XRD) patterns were obtained with a diffractometer, scanning samples from 10º to 80º (2θ) using the Bruker DX-5

instrument. The surface morphology was investigated using scanning electron microscopy (Zeiss Germany 300 scanning electron microscope) at an accelerating voltage of 5.0 to 15 kV for different magnifications. The transmission electron microscopy study was performed to analyze the microstructure (HRTEM, HT-7700, Hitachi, Japan). The UV-DRS spectrum was measured with a Shimadzu 2600R, using barium sulfate as reference in the 200-800 nm range. The optical band gap (E_g) of the nanocomposite was estimated by converting reflectance data to absorbance by the Kubelka-Munk equation:

RESULTS AND DISCUSSION

XRD studies: The XRD pattern of the annealed $MgFe_2O_4/TiO_2/ZnO$ nanocomposite powder are shown in Fig. 1, with diffraction lines labeled by Miller indices. The patterns confirm the presence of $MgFe_2O_4$ (JCPDS card no. 743-1720), TiO_2 (JCPDS card no. 21-1272 and 21-1276) and ZnO (JCPDS card no. 36-1451). The observed 2θ values are 25º, 28º, 36º, 41º, 45º, 49º, 55º, 58º, 64º, 69º and 70º. The peaks at 36º, 58º and 64º correspond to the planes (311), (333) and (440), respectively indicating the presence of magnesium ferrite. while the peaks at 25º and 55º correspond to planes (101) and (105), respectively indicate the presence of titanium dioxide. Similarly, the peaks at 49º and 56º correspond to the planes (102) and (110), respectively confirmed the presence of ZnO. The intense peaks in the diffractogram also confirmed the crystallinity of the prepared nanocomposite.

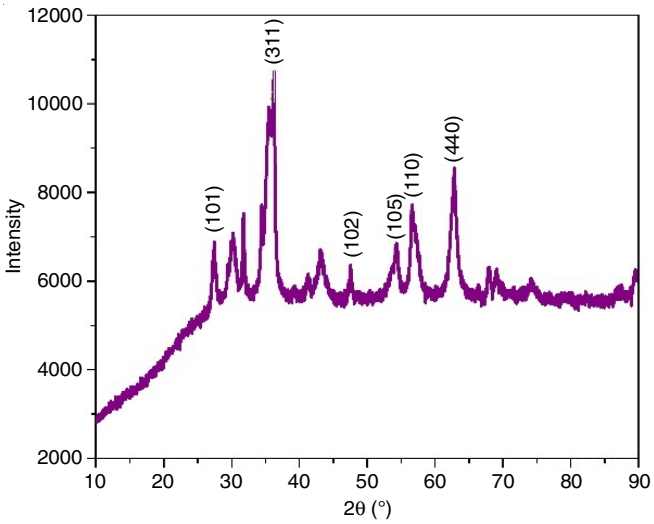

Fig. 1. XRD of $MgFe_2O_4/TiO_2/ZnO$

UV-DRS studies: Fig. 2a displays a UV-Vis diffuse reflectance spectrum (DRS) for the prepared $MgFe_2O_4/ZnO/TiO_2$. nanocomposite. The UV-Vis spectrum exhibits a significant decline in reflectance from 300 to 400 nm, probably due to the overlapping with the material's absorption edge. This type of analysis is commonly used to study the optical properties of photocatalysts, providing insights into both absorption and reflectance behaviour across the UV and visible light spectrum [23]. The optical band gap (E_g) of the nanocomposite was estimated by converting reflectance data to absorbance by the Kubelka-Munk equation:

$$F(R_\infty) = \frac{(1-R_\infty)^2}{2R_\infty}$$

The E_g can be obtained from tauc equation:

$$[h\nu \cdot F(R_\infty)]^{1/n} = A(h\nu - E_g)$$

where h is Planck constant, ν is the frequency of vibration, A is the proportional constant, $F(R_\infty)$ is the Kubelka-Munk function, and n represent the nature of the sample's transition, n = 1/2 for direct and n = 2 for indirect transition. The E_g can be obtained from a tauc plot by plotting $[h\nu \cdot F(R_\infty)]^{1/n}$ against the energy in electron volt.

The linear portion of the Tauc plot was extrapolated to intersect the energy axis at approximately 2.2927 eV, indicating the optical band gap of the ternary nanocomposite (Fig. 2b).

Morphological studies

SEM and EDAX: The SEM images (Fig. 3a-c) display the morphology of ternary nanocomposite at varying magnifi-

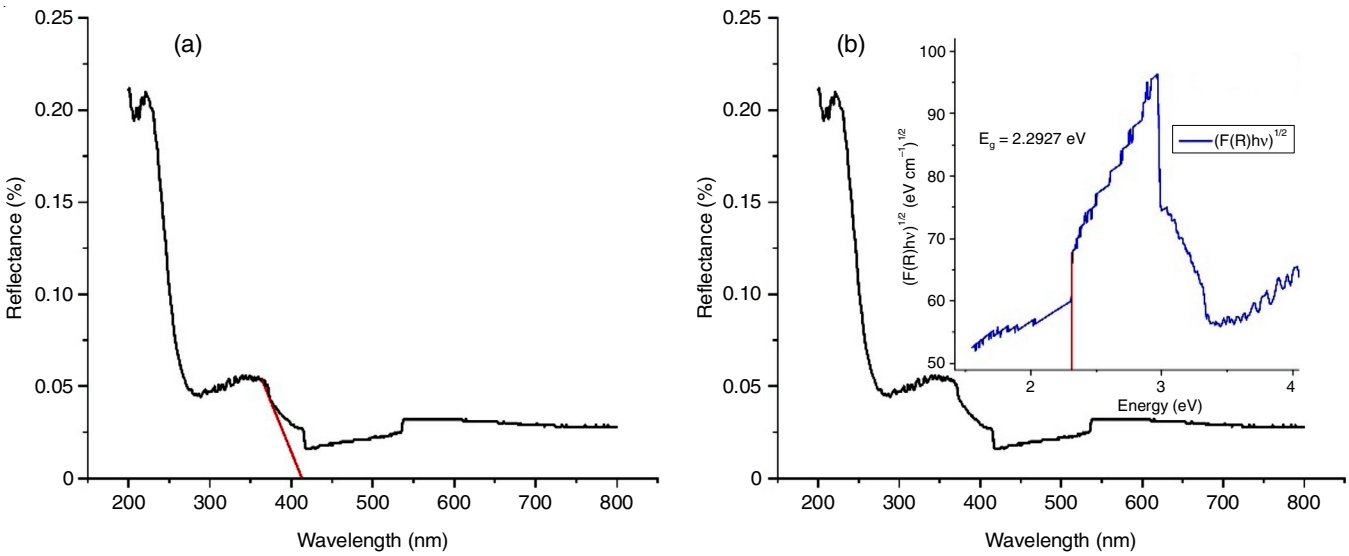

Fig. 2. UV-visible absorption spectra of $MgFe_2O_4/TiO_2/ZnO$ (a) and Band gap of $MgFe_2O_4/TiO_2/ZnO$ (b)

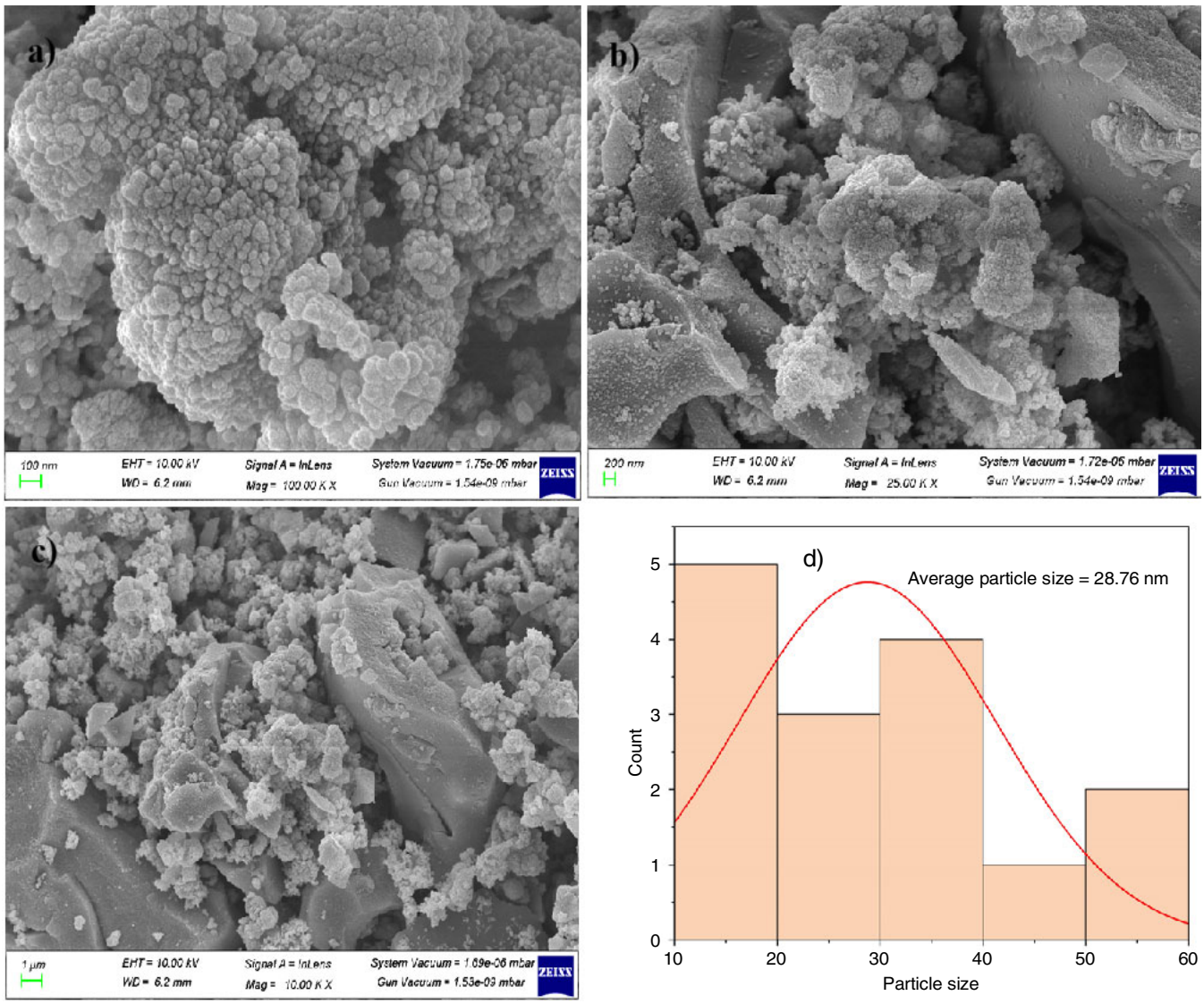

Fig. 3. SEM images of $MgFe_2O_4/TiO_2/ZnO$ (a) 100 nm (b) 200 nm (c) 1 µm (d) particle size distribution of $MgFe_2O_4/TiO_2/ZnO$ (SEM)

cations, revealing small and aggregated particles. The texture appears rough and porous with a visible mixture of small and larger particles. The particle size distribution histogram (Fig. 3d) provides a quantitative analysis of particle sizes, with an average size of around 28 nm. The SEM images clearly confirm the histogram, demonstrating the actual appearance and size of the prepared nanocomposite.

The EDS spectrum of ternary $MgFe_2O_4/TiO_2/ZnO$ nanocomposite showed the existence of O, Mg, Ti, Fe and Zn elements with the composition of 6.76, 0.79, 12.73, 73.76 and 5.95%, respectively (Fig. 4). This further authenticated FT-IR and XRD results and confirmed the formation of the ternary nanocomposite.

TEM studies: The TEM images of the ternary nanocomposite, with individual particles marked by their dimensions, ranging from about 10 nm to 50 nm (Fig. 5a-b). The variation in the particle size and morphology revealed a clustered or aggre-gated structure of nanoparticles within the sample. The presence of concentric rings in Fig. 5c suggested that the nanocomposite is polycrystalline in nature and the spacing between

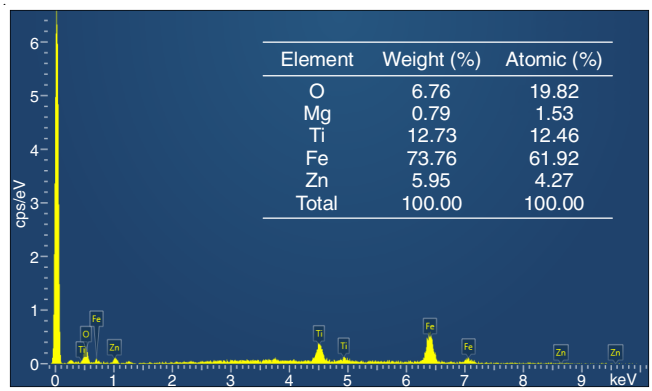

Element	Weight (%)	Atomic (%)
O	6.76	19.82
Mg	0.79	1.53
Ti	12.73	12.46
Fe	73.76	61.92
Zn	5.95	4.27
Total	100.00	100.00

Fig. 4. EDX spectrum of $MgFe_2O_4/TiO_2/ZnO$

the rings corresponds to the specific crystallographic planes. The particle size distribution histogram, similar to the previous image, indicates an average particle size of around 38 nm.

FT-IR studies: The FTIR spectrum of the synthesized $MgFe_2O_4/TiO_2/ZnO$ nanocomposites is shown in Fig. 6. The OH stretching peaks are appeared in the 3977-3561 cm^{-1}

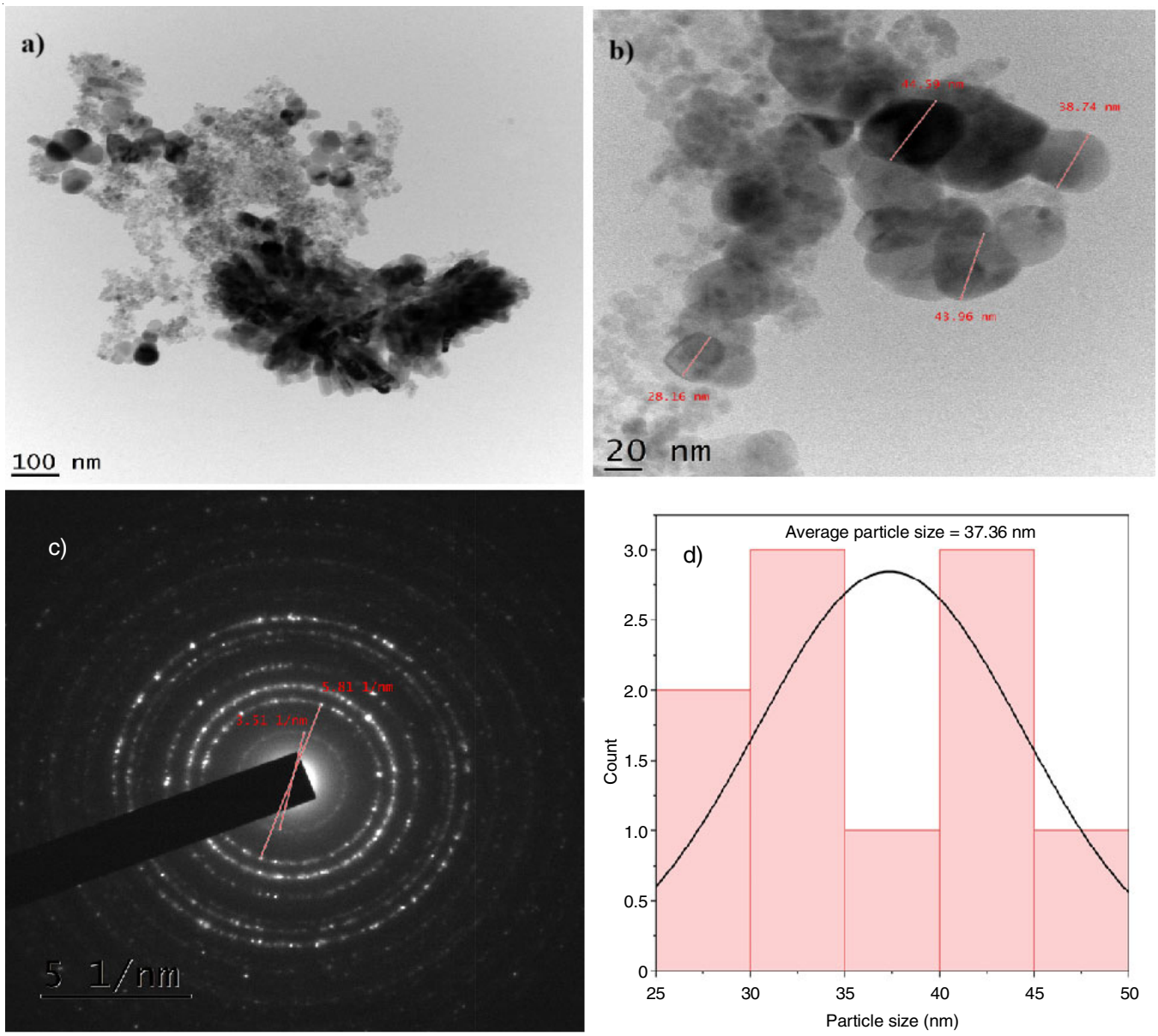

Fig. 5. (a,b,) TEM images of $MgFe_2O_4/ZnO/TiO_2$, (c) SAED pattern of $MgFe_2O_4/ZnO/TiO_2$, (d) particle size distribution of $MgFe_2O_4/ZnO/TiO_2$

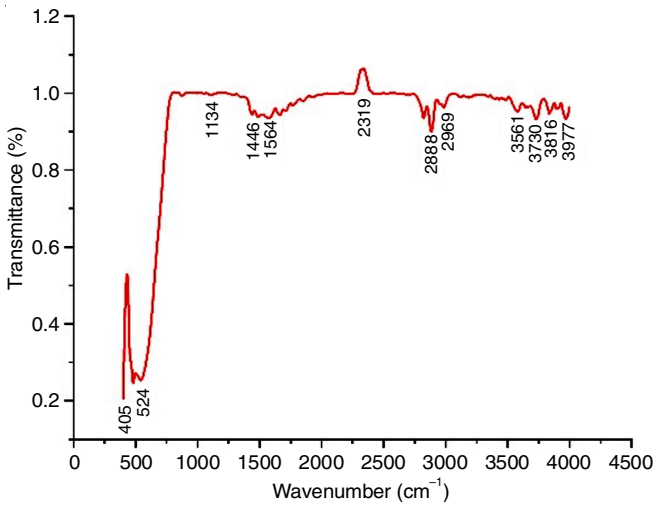

Fig. 6. FTIR spectrum of $MgFe_2O_4/ZnO/TiO_2$

region, while the OH bending peak is at 1134 cm^{-1}. The peak at 2969 cm^{-1} is associated with the CH stretching, whereas the peak at 2319 cm^{-1} is attributed to the hydrogen bonding involving oxygen containing groups. The peak at 405 cm^{-1} (Ti-O bonds) and 524 cm^{-1} (Zn-O) are typically associated with the metal-oxygen (M-O) stretching vibrations, indicating the presence of metal oxides. Moreover, band at 1446 cm^{-1} corresponds to Ti-O-Ti bonding and demonstrated the stretching modes of hydroxyl groups on the surface of the photocatalyst, suggesting that the enhanced peaks contribute to its good photocatalytic activity.

Magnetic properties: At room temperature, the magnetic properties of the material were examined using a vibrating sample magnetometer (VSM). Fig. 7 suggests a ferromagnetic or ferrimagnetic material, as the curve shows a clear response to the applied magnetic field, with the magnetic moment not

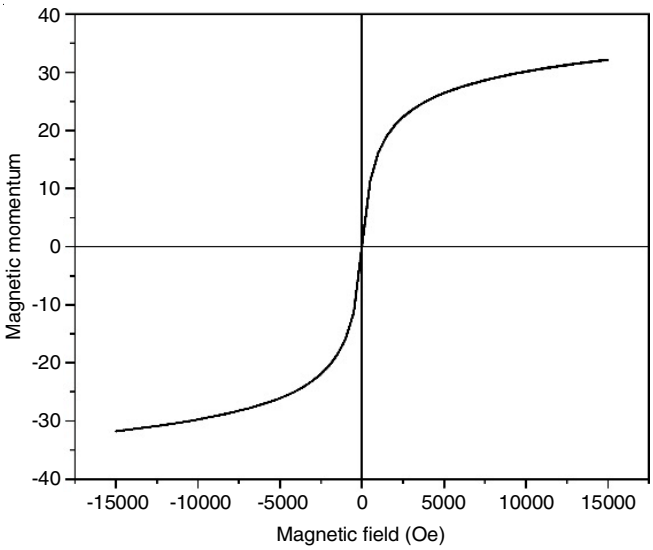

Fig. 7. Magnetization loop for $MgFe_2O_4/ZnO/TiO_2$ composite at room temperature

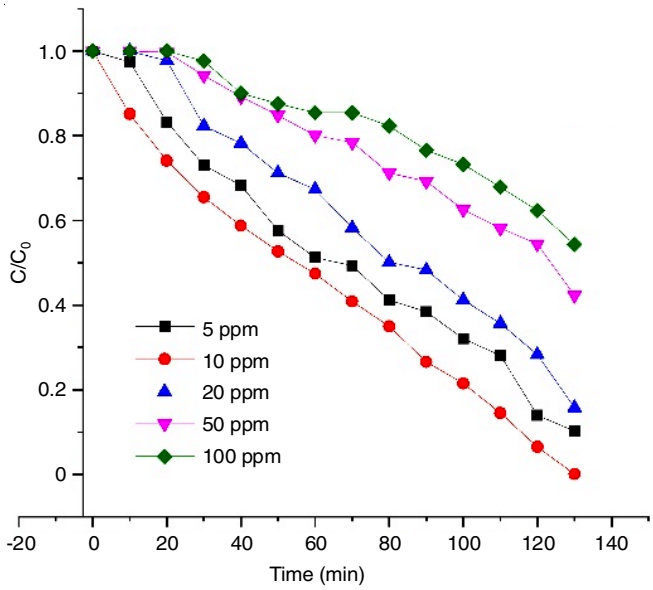

Fig. 8. Effect of initial dye concentration on the photocatalytic degradation of eosin Y dye

returning to zero as the field is reduced doping with magnesium reduced the magnetic value from 60 emu for pure magnesium ferrite to 32.12 emu. As the magnetic field increases, the magnetic moment reaches a saturation point, where the material can no longer be further magnetized. The loop shows a non-linear path, indicating some level of magnetic hysteresis.The resulting nanocomposite exhibits heterogeneous magnetic catalytic properties, which is essential for reusable and regenerative materials.

Photocatalytic efficiency: To determine the optimal conditions for the effective photocatalytic degradation of eosin Y (EY) dye, the effects of various parameters such as pH, irradiation, temperature, catalyst dose and initial dye concentration were investigated by varying one parameter at a time while keeping the others constant.

Effect of initial dye concentration: The photocatalytic efficacy of the ternary nanocomposite ($MgFe_2O_4/TiO_2/ZnO$) was tested by changing the dye content from 5 mg/L to 100 mg/L while keeping the solution pH at 6 and catalyst loading at 10 mg/L. At a concentration of 10 mg/L, the eosin Y dye was completely degraded within 130 min (Fig. 8). At larger concentrations, the degradation rate reduced due to the blanket effect, where surplus eosin Y dye molecules cover the active areas on the catalyst surface and reduce the production of OH radicals. However, as the catalyst dosage was fixed at 10 mg/L, there was insufficient reactive species (OH radicals) to compensate for the increased eosin Y dye molecules. Another factor contributing to lower efficiency at greater concentrations is the visible light screening activity of the eosin Y dye, which further inhibits the photocatalytic process.

Effect of pH: The pH of the solution affects the efficiency of the photocatalytic activity to a greater extent. To investigate this, the pH was adjusted from 4 to 7 using 0.1 M HCl and/or NaOH solutions. Eosin Y dye was exposed to visible light for 100 min while keeping other parameters constant and the results shown in Fig. 9 indicated that the degradation rate is highest at pH 6 and pH 7.

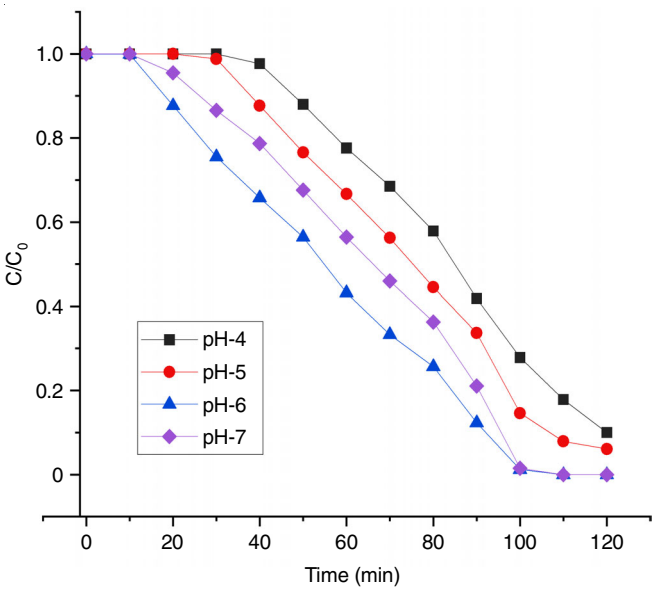

Fig. 9. Effect of pH on the photocatalytic degradation of eosin Y dye

Effect of temperature: The effect of adsorption temperature on EY dye removal by nanocomposites was studied between 25 and 40 ºC. As the temperature increased from 40 ºC, the percentage of eosin Y dye adsorbed increased from comp-lete degradation. The concentration and pH of the dye solution were kept constant at 10 mg/L and pH 6 and 7, respectively. The highest adsorption capacity and degradation efficiency (100%) were observed at 40 ºC after 80 min (Fig. 10). The results show that the adsorption mechanism is endothermic, signifying that higher temperatures accelerate EY dye adsorption on the adsorbent.

Effect of catalyst loading: To examine the effect of ternary nanocomposite concentration on the photocatalytic degradation of EY dye under visible light, the nanocomposite concentration was varied from 0.25 g/L to 0.55 g/L, with the solution pH kept at 6 and 7 and the initial concentration of

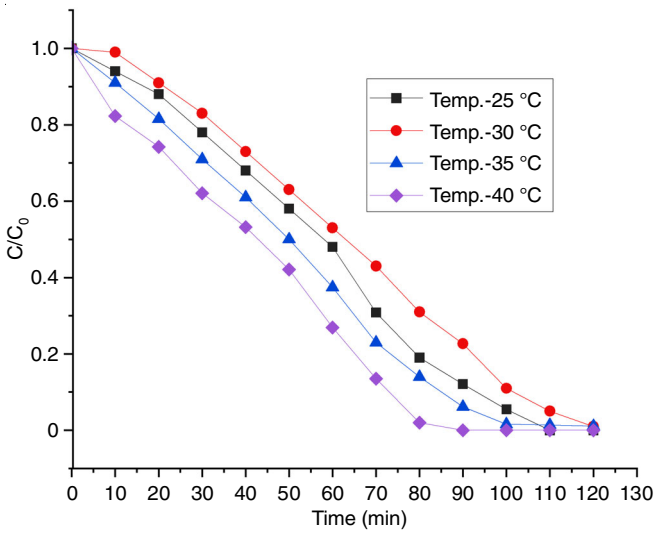

Fig. 10. Effect of temperature on the photocatalytic degradation of eosin Y dye

eosin Y dye at 0.45 g/L. As the catalyst concentration increased up to 0.55 g/L, the degradation rate of eosin Y dye improved over 60 min (Fig. 11). However, further increases in catalyst concentration led to a decrease in the degradation rate, which may be due to increased turbidity and agglomeration of catalyst particles, which hinder light penetration and reduce the number of active sites available for light absorption.

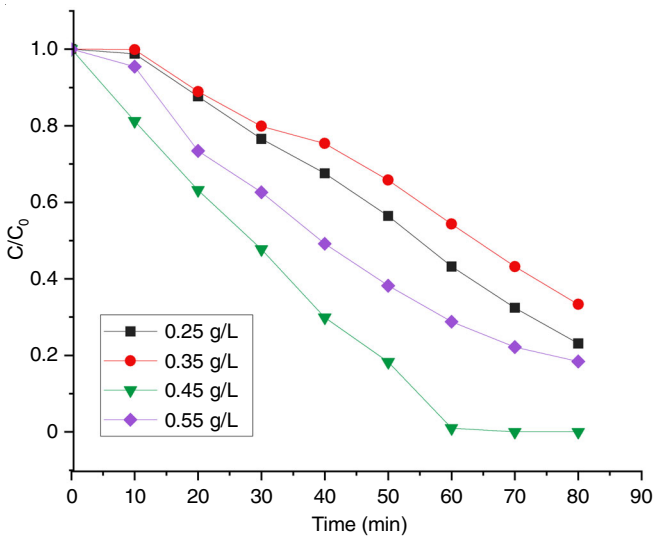

Fig. 11. Effect of catalyst dosage on the photocatalytic degradation of eosin Y dye

Effect of irradiation time: The absorption spectrum of EY dye under solar photocatalysis with $MgFe_2O_4/TiO_2/ZnO$ catalyst was analyzed. The intensity of the absorption peak at 520 nm decreased progressively with the duration of catalysis. Fig. 12 shows the photocatalytic degradation efficiency (C_t/C_0 *vs.* time) for the catalysts studied. After 60 min, the ternary nanocomposite as photocatalyst achieved a maximum EY degradation of 100%, demonstrating their high photocatalytic activity. In contrast, when EY dye was exposed to sunlight without a catalyst, the degradation was significantly lower, highlighting the effectiveness of the prepared photocatalyst.

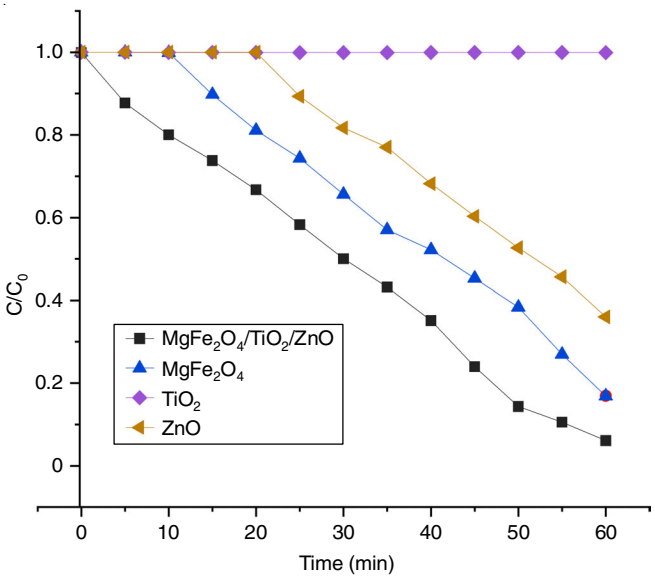

Fig. 12. Effect of irradiation time on the photocatalytic degradation of eosin Y dye

Study on reusability and regenerability: To minimize costs and ensure that photocatalysts are both effective and environmentally safe by reducing the release of secondary pollutants, it is important to test their reusability before industrial application. The reusability of the spent photocatalysts was assessed as shown. The photocatalyst was centrifuged, cleaned and then tested for performance across three cycles, demonstrating consistent efficiency. Similarly, as depicted in Fig. 13, the photocatalyst maintained high effectiveness over three consecutive cycles of eosin Y dye degradation. After three cycles, the photodegradation efficiency decreased to 70 % for EY dye.

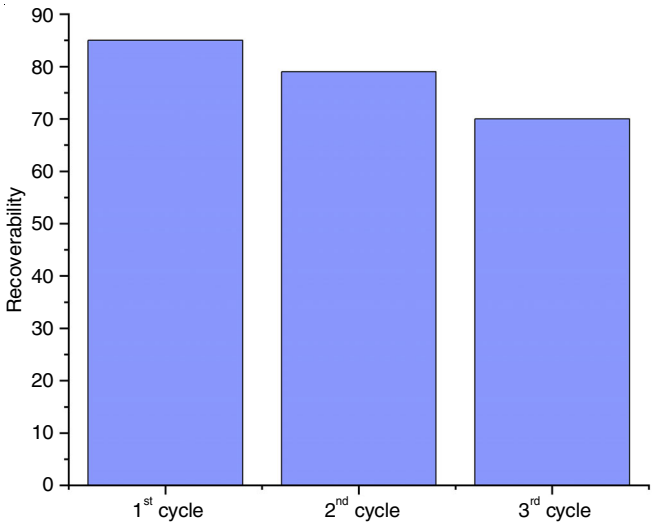

Fig. 13. Reusability of eosin Y dye

Antibacterial activity: The antibacterial activity of the prepared ternay nanocomposite was evaluated using the disc diffusion method. The ternary nanocomposite ($MgFe_2O_4/TiO_2/$

ZnO) effectively inhibited the growth of both Gram-positive (*Firmicutes*) and Gram-negative (*Aeromonas*) bacteria. The nanocomposite demonstrated stronger inhibition against Gram-negative strains as compared to Gram-positive bacteria (Table-1). The increased effectiveness against Gram-negative bacteria is attributed to the structural differences in their cell walls. The thinner cell wall of Gram-negative bacteria facilitates the easier penetration of small nanocomposite particles, resulting in the generation of reactive oxygen species (ROS) inside the cell. The ROS interact with cellular components, causing damage to genetic material and proteins, ultimately leading to bacterial cell death.

TABLE-1
ANTIBACTERIAL ACTIVITY DATA OF TERNARY $MgFe_2O_4/TiO_2/ZnO$ NANOCOMPOSITE

Sample	Conc. (µg/mL)	*Firmicutes* (Gram-positive) (mm)	*Aeromonas* (Gram-negative) (mm)
$MgFe_2O_4/TiO_2/ZnO$ nanocomposite	20	4	5
	80	5	8
	150	9	11
	200	14	15

Conclusion

This work presents the synthesis and characterization of ternary $MgFe_2O_4/TiO_2/ZnO$ nanocomposite using the sol-gel method. The prepared nanocomposite displayed the lowering of band gap and enhanced photodegradation under both visible and UV light irradiation. Its photocatalytic activity was successfully analyzed against eosin Y dye under UV visible light irradiation, which confirmed that the material has excel-lent potential in actual contaminated water treatment. Finally, the prepared nanocomposite is also found to be efficient anti-bacterial agents against Gram-negative (*Aeromonas*) bacteria.

ACKNOWLEDGEMENTS

The authors express their gratitude to Advanced Analytical Laboratory, Andhra University for providing the spectral analysis facilities.

CONFLICT OF INTEREST

The authors declare that there is no conflict of interests regarding the publication of this article.

REFERENCES

1. M. Kocijan, L. Curkovic, D. Ljubas, K. Mu•ina, I. Baèic, T. Radoševic, M. Podlogar, I. Bdikin, G. Otero-Irurueta, M.J. Hortigüela and G. Gonçalves, *Appl. Sci.*, **11**, 3966 (2021); https://doi.org/10.3390/app11093966
2. C.V. Tran, D.D. La, P.N. Thi Hoai, H.D. Ninh, P.N. Thi Hong, T.H.T. Vu, A.K. Nadda, X.C. Nguyen, D.D. Nguyen and H.H. Ngo, *J. Hazard. Mater.*, **420**, 126636 (2021); https://doi.org/10.1016/j.jhazmat.2021.126636
3. R. Farouq, E.K. Ismaeel and A.M. Monazie, *J. Fluoresc.*, **32**, 715 (2022); https://doi.org/10.1007/s10895-022-02889-3
4. A.H. Ali, A.A. Risn and A. Hussein, *IOP Conf. Series: J. Phys*., **1032**, 012008 (2018); https://doi.org/10.1088/1742-6596/1032/1/012008
5. M.S. Nawaz and M. Ahsan, *Alex. Eng. J.*, **53**, 717 (2014); https://doi.org/10.1016/j.aej.2014.06.007
6. S. Shareef and A. Mushtaq, *Int. J. Chem. Biochem. Sci.*, **24**, 278 (2023).
7. V. Russo, M. Hmoudah, F. Broccoli, M.R. Iesce, O.-S. Jung and M. Di Serio, *Frontiers Chem. Eng.*, **2**, 581487 (2020); https://doi.org/10.3389/fceng.2020.581487
8. D.-E. Lee, M.-K. Kim, M. Danish and W.-K. Jo, *Catal. Commun.*, **183**, 106764 (2023); https://doi.org/10.1016/j.catcom.2023.106764
9. A. Chakravorty and S. Roy, *Sustain. Chem. Environ.*, **8**, 100155 (2024); https://doi.org/10.1016/j.scenv.2024.100155
10. I.A. Alsafari, R. Fatima, M.F. Warsi, I. Ayman, A. Jamil, M. Shahid and A. Irshad, *J. Taibah Univ. Sci.*, **16**, 1016 (2022); https://doi.org/10.1080/16583655.2022.2135812
11. J. Wang, T. Hasegawa, Y. Asakura and S. Yin, *Catalysts*, **12**, 1568 (2022); https://doi.org/10.3390/catal12121568
12. P.L. Meena, K. Poswal, A.K. Surela and J.K. Saini, *Water Sci. Technol.*, **84**, 2615 (2021); https://doi.org/10.2166/wst.2021.431
13. J. Panda, U.P. Singh and R. Sahu, *IOP Conf. Series: Mater. Sci. Eng*., **410**, 012008 (2018); https://doi.org/10.1088/1757-899X/410/1/012008
14. A.B. Younis, V. Milosavljevic, T. Fialova, K. Smerkova, H. Michalkova, P. Svec, P. Antal, P. Kopel, V. Adam, L. Zurek and K. Dolezelikova, *BMC Microbiol.*, **23**, 207 (2023); https://doi.org/10.1186/s12866-023-02955-1
15. M.M. Ali, M.J. Haque, M.H. Kabir, M.A. Kaiyum and M.S. Rahman, *Results Mater.*, **11**, 100199 (2021); https://doi.org/10.1016/j.rinma.2021.100199
16. D. Suresh, R.M. Shobharani, P.C. Nethravathi, M.A. Pavan Kumar, H. Nagabhushana and S.C. Sharma, *Spectrochim. Acta A Mol. Biomol. Spectrosc.*, **141**, 128 (2015); https://doi.org/10.1016/j.saa.2015.01.048
17. M.A. Habib, M.T. Shahadat, N.M. Bahadur, I.M.I. Ismail and A.J. Mahmood, *Int. Nano Lett.*, **3**, 5 (2013); https://doi.org/10.1186/2228-5326-3-5
18. W. DeGroat, H. Abdelhalim, K. Patel, D. Mendhe, S. Zeeshan and Z. Ahmed, *Sci. Rep.*, **14**, 1 (2024); https://doi.org/10.1038/s41598-023-50600-8
19. H.A. Patehkhor, M. Fattahi and M. Khosravi-Nikou, *Sci. Rep.*, **11**, 24177 (2021); https://doi.org/10.1038/s41598-021-03492-5
20. A. Tabasum, I.A. Bhatti, N. Nadeem, M. Zahid, Z.A. Rehan, T. Hussain and A. Jilani, *Water Sci. Technol.*, **81**, 178 (2020); https://doi.org/10.2166/wst.2020.098
21. M. Ben Arbia, H. Helal and E. Comini, *Nanomaterials*, **14**, 359 (2024); https://doi.org/10.3390/nano14040359
22. N.I. Ermokhina, V.V. Shvalagin, N.I. Romanovska, P.A. Manoryk, R.Yu. Barakov, M.O. Kompanets, V.I. Sapsay, D.O. Klymchuk and A.M. Puziy, *SN Appl. Sci.*, **3**, 491 (2021); https://doi.org/10.1007/s42452-021-04474-y
23. S. Panwar, V. Kumar and L.P. Purohit, *Sci. Rep.*, **14**, 21341 (2024); https://doi.org/10.1038/s41598-024-72186-5